

# High-performance real-world optical computing trained by in situ model-free optimization

GUANGYUAN ZHAO<sup>1,2,3</sup> AND XIN SHU<sup>1,2</sup>

<sup>1</sup>Department of Biomedical Engineering, the Chinese University of Hong Kong, Hong Kong, China

<sup>2</sup>Equal contribution

<sup>3</sup>zhaoguangyuan@link.cuhk.edu.hk

Compiled November 6, 2023

Optical computing systems can provide high-speed and low-energy data processing but face deficiencies in computationally demanding training and simulation-to-reality gap. We propose a model-free solution for lightweight in situ optimization of optical computing systems based on the score gradient estimation algorithm. This approach treats the system as a black box and back-propagates loss directly to the optical weights' probabilistic distributions, hence circumventing the need for computation-heavy and biased system simulation. We demonstrate a superior classification accuracy on the MNIST and FMNIST datasets through experiments on a single-layer diffractive optical computing system. Furthermore, we show its potential for image-free and high-speed cell analysis. The inherent simplicity of our proposed method, combined with its low demand for computational resources, expedites the transition of optical computing from laboratory demonstrations to real-world applications.

<http://dx.doi.org/XX.XXXXXX>

## 1. INTRODUCTION

Optical computing leverages the properties of light waves to facilitate high-speed data processing while reduces the energy cost [1–5], such as the optical spatial correlators [3, 6], the optical edge detector [7]. Recent advance in automatic differentiation has enabled in silico training of large-scale optical computing weights, giving rise to the realizations of diffractive neural networks [8, 9], optical reservoir computing [10, 11] and coherent nanophotonic circuits [12].

Training optical computing systems presents two significant challenges: an intensive computational process and a performance disparity between simulation and reality when implementing pre-trained weights onto real-world systems [9, 13, 14]. The systems are typically trained in silico using differentiable simulators rooted in the first principle of optics, an approach known as simulator-based training (SBT). While SBT has proven effective within the confines of the simulator, the performance in real systems is largely contingent upon the simulator's fidelity. Factors such as misalignment and aberration, often omitted in simulations, can cause significant performance degradation when weights trained exclusively within the simulator are applied to real-world systems. To bridge the simulation-to-reality gap, physics-aware training (PAT) and hybrid training (HBT) have been introduced [15, 16]. Both training strategies include conducting the forward pass in the real system and

back-propagating loss through the simulator. Consequently, the error measured in the real system during the forward pass refines weight optimization more accurately than strictly in silico training [13].

Despite these advances, there is a continued reliance on a physics-based simulator during the backward process in the current in situ training methods. Such a setting brings three drawbacks: Firstly, the biased simulator prohibits the above training process from achieving optimal results; Secondly, the in silico simulation requires large memory and computation, limiting the aforementioned methods from in situ training in edge devices with limited computing resources [17]; Lastly, the model-based training strategies require the input object to be fully visible during the training. Capturing the high-fidelity image of this object would impose burdens on the experiment.

Here we propose an alternative solution to the above solutions requiring back-propagating errors through the simulator: an in situ, model-free optimization (MFO) method using a score gradient estimation algorithm [18, 19] to solely use the forward outputs from the real system to get gradient for updating the weights of the optical computing system. As shown in Fig. 1, our method treats the optical system as a black box and back-propagates task-specific negative-loss as rewards to the source weight distributions (Fig. 1b). This process only requires knowledge of the weights and forward outputs of the optical com-

	SBT [9]	HBT [16]	MFO (ours)
In situ	No	Yes	Yes
Computation overhead	High	High	Low
Model-free	No	No	Yes

**Table 1. Comparison of strategies on training optical computing systems** along the axes of in situ training capability (in situ), in silico computation overhead (computation overhead), and requirements on a physics-based simulator and knowledge of input objects (model-free).

puting system, unlike the SBT and HBT methods that require a model and the images of the input objects (Fig. 1a). A tabular comparison of our work and the prior methodologies is in Tab. 1.

We demonstrate our method on a home-built single-layer diffractive optical computing system. Experimental results show that our MFO method outperforms the result of hybrid training on the commonly used MNIST and FMNIST datasets [9, 15, 16] (Sec. 3A). As a proof-of-concept demonstration, we experimentally show that our MFO-trained optical computing system can achieve classification of white blood cell phase maps with a testing accuracy of 73.8% (Sec. 3B), making it a promising method for image-free and high-speed cell analysis. Lastly, we show our pipeline only consumes  $\sim \frac{1}{1000}$  computing resources as compared to the HBT in situ methods by avoiding computation-intensive modeling of the wave propagation process (Sec. 3C).

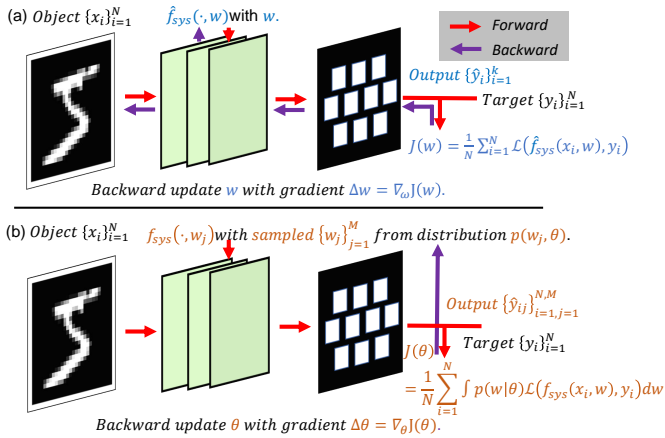


**Fig. 1. Model-free training of the optical computing system.** (a) The blue highlights shows that the conventional training of the optical computing system relies on a physics-based simulator  $\hat{f}_{sys}$ , which substitutes the inaccessible  $f_{sys}$  corresponding to the real system. The training process back-propagates the loss through simulator  $\hat{f}_{sys}$  to update the weight  $w$ . This is the basis of SBT and HBT methods. (b) The brown highlights shows that our model-free training strategy back-propagates the error of training to the distribution parameter  $\theta$  and bypasses the reliance on correct differentiable modeling of the optical system  $f_{sys}$  and knowledge on input  $\{x_i\}_{i=1}^N$ .

## 2. METHODOLOGY

In what follows, we detail the problem setup of training the optical computing system and our solution. We introduce background and problem formation in Subsec. A and the conven-

tional solution of using simulator-based training (SBT) in Subsec. B. We then illustrate our solution to the problem, the model-free optimization (MFO) for training the optical computing system in Subsec. C. Finally, we illustrate the optical computing system and its simulator in Subsec. D, which we will use to demonstrate the performance of our method.

### A. Problem setup

We are interested in learning the optimal optical weights  $w \in \mathbb{R}^H$  for the optical computing system on desired task with training dataset  $\mathcal{D} = \{x_i, y_i\}_{i=1}^N$ , where  $N$  is the size of the dataset,  $H$  is the number of trainable parameters in  $w$ , and  $x$  and  $y$  denote the input and target of interest, respectively. A function  $f_{sys}(\cdot; w)$  maps  $x \rightarrow y$  through this optical computing system with  $w$ . Specifically, in the image classification task based on the diffractive optical computing system we work on,  $f_{sys}$  denotes the optical mapping from the input image  $x$  to the output label  $y$ , and  $w$  is the phase-valued optical computing weight.

During training, we minimize the cost function  $J(w)$  as the expected value across the entire training data set  $\mathcal{D}$ :

$$w^* = \arg \min_w J(w), \quad (1a)$$

$$= \arg \min_w \mathbb{E}[\mathcal{L}(\mathcal{D}, w)], \quad (1b)$$

$$= \arg \min_w \frac{1}{N} \sum_{i=1}^N \mathcal{L}(f_{sys}(x_i; w), y_i), \quad (1c)$$

where  $\mathcal{L}$  is the task-specific loss function, we use cross-entropy loss [20] since we deal with image classification tasks throughout this paper.

We use gradient descent-based search to find optimal  $w$  to minimize the objective function  $J(w)$ :

$$w = w - \alpha \nabla_w J(w), \quad (2)$$

where  $\nabla_w$  represents the gradient operator that collects all the partial derivatives of a function concerning parameters in  $w$ , and  $\alpha$  is the learning rate.

It is straightforward to use the backpropagation method [14] to take the gradient through  $f_{sys}$  and finds the gradient  $\nabla_w J(w)$  as:

$$\nabla_w J(w) = \frac{1}{N} \sum_{i=1}^N \nabla_w \mathcal{L}(f_{sys}(x_i, w), y_i), \quad (3)$$

when we have an accurate differentiable modeling of  $f_{sys}$ . However, this is the case for digital neural networks, but not when we train a real-world optical computing system. **Thus, this paper's critical aim is finding an accurate gradient estimation of  $\nabla_w J(w)$  to update optical computing weights  $w$  in a real-world system.**

### B. In silico simulator-based training (SBT)

**Back-propagate through the simulator  $\hat{f}_{sys}$ .** In a real-world optical computing system, since we do not have an exact functional expression of  $f_{sys}$ , the **simulator-based training** builds a simulator  $\hat{f}_{sys}$  as the differentiable approximation of  $f_{sys}$  for the simulation-based training (Fig. 1a). The naive training strategy is substituting  $f_{sys}$  in Eq. 3 with the simulator  $\hat{f}_{sys}$ , applying in silico training on the simulator:

$$\nabla_w J(w) = \frac{1}{N} \sum_{i=1}^N \nabla_w \mathcal{L}(\hat{f}_{sys}(x_i, w), y_i). \quad (4)$$

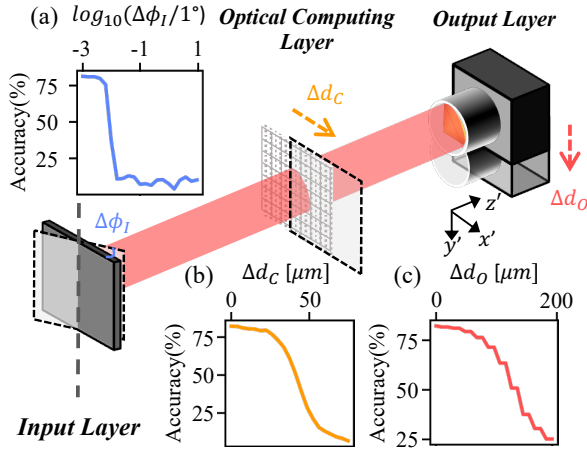


**Fig. 2. System misalignment in a real optical computing system degenerates the performance of the optical computing system trained solely with a physics-based simulator.** (a) Accuracy drops to 36.4% from 82.2% when having a misaligned rotation angle  $\Delta\phi_I = 0.01^\circ$ . (b) Accuracy drops to 51.0% from 82.2% when the  $x'$ -axis misalignment of the optical computing layer  $\Delta d_c$  is  $41.1 \mu\text{m}$ . (c) Accuracy decreases to 50.9% from 82.2% when the  $y'$ -axis misalignment of the output layer  $\Delta d_o$  is  $62.4 \mu\text{m}$ .

Result of  $\nabla_w J(w)$  is used in Eq. 2 to update the parameter  $w$ . After training, the optimized  $w$  is uploaded to the real optical computing system  $f_{\text{sys}}$  to test the performance.

**Simulation-to-reality gap.** The aforementioned simulator-based training is based on backpropagation through the simulator  $\hat{f}_{\text{sys}}$ . The "sim2real" gap is low (i.e., the gradient  $\nabla_w J(w)$  is an accurate estimation) when the simulator  $\hat{f}_{\text{sys}}$  is similar to  $f_{\text{sys}}$ . However, this assumption does not hold in many prototypes of optical computing systems where the inadequate modeling and misalignment between the optical elements decay the performance of the SBT during the "sim2real" transfer. We use a simulator described in Subsec. D to assess the adverse effect of misalignment on the image classification results by measuring drops in classification accuracy when introducing various misalignments to a well-trained ideal optical computing system. For instance, we show with simulations in Fig. 2 that slightly laterally misaligning the optical computing layer by  $41.1 \mu\text{m}$  reduces the classification accuracy by 31.2%.

### C. In situ model-free optimization (MFO)

Our solution for solving the aforementioned "sim2real" gap issue in Subsec. B is: in situ learning the optical weights  $w$  with the model-free optimization. In situ learning, on the one hand, enables us to access the output of  $f_{\text{sys}}$  and, on the other hand, in principle, feasible on the hardware requirement side as we can use spatial light modulators as programmable devices to update optical weights  $w$ . The challenging part is designing a training strategy that efficiently uses the actual system function  $f_{\text{sys}}$  to construct an unbiased gradient estimator. Here, we use the score gradient estimator to calculate the gradient [21, 22] for the backward update of parameters in  $w$  while circumventing the construction of  $\hat{f}_{\text{sys}}$ , a biased and resource-intensive numerical modeling of  $f_{\text{sys}}$ .

**Back-propagate through the weights distribution  $p$ .** In our score gradient estimation for model-free optimization, we model optical computing weights  $w$  as a random variable that follows

a parameterized distribution:  $w \sim p(w|\theta)$  and rewrite the objective function in Eq. 1c as a probabilistic objective function:

$$\begin{aligned} \arg \min_{\theta} J(\theta) &= \arg \min_{\theta} \frac{1}{N} \sum_{i=1}^N \mathbb{E}_{p(w|\theta)} [\mathcal{L}(f_{\text{sys}}(x_i, w), y_i)], \quad (5a) \\ &= \arg \min_{\theta} \frac{1}{N} \sum_{i=1}^N \int p(w|\theta) \mathcal{L}(f_{\text{sys}}(x_i, w), y_i) dw. \quad (5b) \end{aligned}$$

The probabilistic distribution  $p(w|\theta)$  is continuous in its domain and differentiable concerning its distributional parameters  $\theta$ . Accordingly, the original goal of optimizing  $w$  is reformulated as finding a most likely distribution  $p(w|\theta)$  that minimizes the objective function in Eq. 5. Specifically, in our work, we model the distribution  $p$  as a multivariate normal distribution with  $\theta = \{\mu, \sigma^2\}$  and  $p(w|\theta) = \mathcal{N}(w; \mu, \sigma^2)$  as we optimize the continuous phase map to be uploaded onto the SLM.

To update distribution parameter  $\theta$  with the gradient descent Eq. 2, we take the gradient on Eq. 5:

$$\nabla_{\theta} J(\theta) = \nabla_{\theta} \frac{1}{N} \sum_{i=1}^N \int p(w|\theta) \mathcal{L}(f_{\text{sys}}(x_i, w), y_i) dw, \quad (6a)$$

$$= \frac{1}{N} \sum_{i=1}^N \int \mathcal{L}(f_{\text{sys}}(x_i, w), y_i) \nabla_{\theta} p(w|\theta) dw, \quad (6b)$$

$$= \frac{1}{N} \sum_{i=1}^N \int p(w|\theta) \mathcal{L}(f_{\text{sys}}(x_i, w), y_i) \nabla_{\theta} \log p(w|\theta) dw, \quad (6c)$$

$$= \frac{1}{N} \sum_{i=1}^N \frac{1}{M} \sum_{j=1}^M \mathcal{L}(f_{\text{sys}}(x_i, w_j), y_i) \nabla_{\theta} \log p(w_j|\theta), \quad (6d)$$

$$= \frac{1}{M} \sum_{j=1}^M \left[ \frac{1}{N} \sum_{i=1}^N \mathcal{L}(f_{\text{sys}}(x_i, w_j), y_i) \right] \nabla_{\theta} \log p(w_j|\theta), \quad (6e)$$

where  $M$  is the number of samples we draw from the distribution  $p(w|\theta)$ . We get  $r(w_j) = \frac{1}{N} \sum_{i=1}^N \mathcal{L}(f_{\text{sys}}(x_i, w_j), y_i)$  as the negative reward corresponding to each weight  $w_j$  sampled from the distribution  $p(w_j|\theta)$ . Equation 6e is the score gradient estimator, where the score function is  $\nabla_{\theta} \log p(w_j|\theta)$ , which has been widely used in other areas, such as policy gradient algorithms in reinforcement learning [19] and diffusion models [23].

**Variance reduction.** The main risk of using such a gradient estimator is the high variance that comes from the Monte Carlo integration step that transits Eq. 6c to Eq. 6d. The Monte Carlo integration step in Eq. 6d approximates the integral value in Eq. 6c by first drawing  $M$  independent samples  $\{w_j\}_{j=1}^M$  from the distribution  $p(w_j|\theta)$  and then computing the average function evaluated in these samples. Such a sampling-based integration step has high variance because different sets of random samples may lead to significantly different integral estimates. We reduce the variance by subtracting the  $r(w_j)$  with baseline value  $\bar{r} = \frac{1}{M} \sum_{j=1}^M r(w_j)$ :

$$\nabla_{\theta} J(\theta) = \frac{1}{M} \sum_{j=1}^M (r(w_j) - \bar{r}) \nabla_{\theta} \log p(w_j|\theta). \quad (7)$$

The subtraction of baseline value in Eq. 7 reduces the variance of gradient estimation while keeping the bias of gradient unchanged [24].

**Training recipe of MFO.** During training, we sample a batch of phase-valued optical computing weights  $\{w_j\}_{j=1}^M$  from the distribution:  $w_j \sim p(w_j|\theta)$ . Then we upload the sampled weights onto the optical computing layer and test the weights with inputs from the dataset  $\mathcal{D}$ . After that, we calculate the rewards and update the distribution parameter  $\theta$  through Eqs. 2 and 7. The algorithm iterates these steps until convergence. After minimizing the objective function Eq. 5, we export  $w_j$  with the smallest  $r(w_j)$  tested on the validation set as the output result of  $w^*$ . In practice, this performs better on training and validation sets than setting  $w^*$  as the sampled mean from the last batch of samples. The algorithmic overview of the training recipe is shown in Algorithm 1.

**Algorithm 1.** Algorithmic overview of MFO.

- 1: **Input:** Classification dataset  $\mathcal{D} = \{x_i, y_i\}_{i=1}^N$ , learning rate  $\alpha$ , number of sampled weights  $M$ , optical computing system  $f_{sys}$ , distribution parameter  $\theta = \{\mu, \sigma^2\}$ , loss function  $\mathcal{L}$ , epochs  $K$ .
- 2: **Output:** Optimized optical computing weight  $w^*$ .
- 3: **for**  $k$  in range  $K$  **do**
- 4:   Sample  $\{w_j\}_{j=1}^M$  from distribution  $p(w_j|\theta)$ .
- 5:   ▷ *in situ evaluate*  $\{w_j\}_{j=1}^M$ .
- 6:   **for**  $j$  in range  $M$  **do**
- 7:      $r(w_j) \leftarrow \frac{1}{N} \sum_{i=1}^N \mathcal{L}(f_{sys}(x_i, w_j), y_i)$ .
- 8:     ▷ *in silico update*  $\theta$ .
- 9:     Calculate  $\Delta\theta$  via Eq. 7.
- 10:     $\theta \leftarrow \theta - \alpha\Delta\theta$ .
- 11:     $w^* \leftarrow w_j$  with the smallest  $r(w_j)$ .

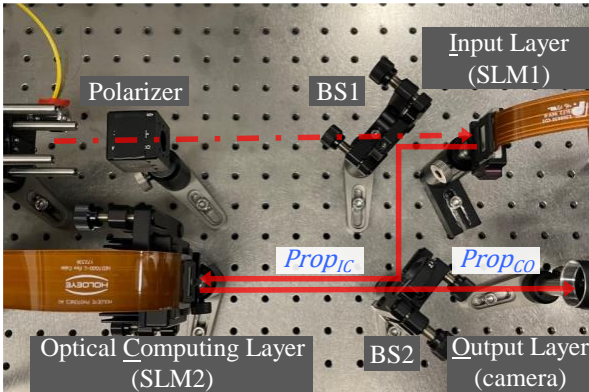


**Fig. 3. Experimental setup of a single-layer optical computing system.** We have a light source incident from the top left, passing through the polarizer and the first beam splitter (BS1), and then reflecting from the input layer which displays phase object by phase delay from the SLM1. The reflected light then passes through BS1 and beam splitter 2 (BS2) and arrives at the optical computing layer, where we use SLM2 to upload the optical processing weights. The reflected light from the modulator then arrives at the output layer, and we calculate the task-specific loss based on the arrival signal. We label the last two paths as  $Prop_{IC}$  and  $Prop_{CO}$ , respectively, in the figure.

## D. Experiment and simulation detail of our diffractive optical computing system

**Experimental setup of the real optical computing system  $f_{sys}$ .** We build our home-built single-layer optical computing system to validate the effectiveness of the proposed training strategy (see Fig. 3). In the experimental setup, we have a laser field  $u_{laser}$  incident onto the input layer with the object field  $u_{obj}$ . The light field reflects from the input layer onto the optical computing layer  $u_w$  and is then detected by the sensor in the output layer. The object and optical computing weights are fulfilled using spatial light modulators (SLMs). Specifically, the length  $d_{IC}$  and  $d_{CO}$  for  $Prop_{IC}$  and  $Prop_{CO}$  in Fig. 3 are 215.1mm and 201.6mm, respectively. The reproducibility of the hardware system is in Supplement Sec. S.1. Since it is difficult to manually align multiple components with high accuracy and we have programmable optical devices, we use digital homography-enabled registration as compensation for manual alignment. More details of digital alignment are given in Supplement Sec. S.5.

**Differentiable physics-based simulator  $\hat{f}_{sys}$ .** We construct an ideal physics-based simulator  $\hat{f}_{sys}$  corresponding to the aforementioned optical computing system  $f_{sys}$  as the sandbox to test different training algorithms. This simulator is also used inside the design loop of SBT and HBT, which serve as the baseline methods to compare with. Since our system only includes free-space wave propagation  $\hat{f}_{prop}$ , wavefront modulation  $\hat{f}_{mod}$ , and sensor detection  $\hat{f}_{det}$ , we build the optical computing simulator by stacking these three optical modules as building blocks. The functions of optical modules are:

$$\hat{f}_{prop}(u_{in}, z) : u_{out} = \mathcal{F}^{-1}(\mathcal{F}(u_{in}) \times \mathcal{F}(h_{prop}(z))), \quad (8a)$$

$$\hat{f}_{mod}(u_{in}, u_{element}) : u_{out} = u_{in} * u_{element}, \quad (8b)$$

$$\hat{f}_{det}(u_{in}) : I_{out} = |u_{in}|^2, \quad (8c)$$

where  $h_{prop}(z) = \frac{e^{ikz'}}{j\lambda z'} e^{\frac{jk}{2z}(x^2+y^2)}$  is the propagation kernel under

Fresnel approximation [25] with a propagation distance  $z'$ , wavelength  $\lambda$  and angular wave number  $k$ ,  $u_{element}$  denotes the wavefront modulation from the programmable optical devices,  $\mathcal{F}$  denotes the Fourier transform.

Based on the modules in Eq. 8, the simulator  $\hat{f}_{sys} = \{\hat{f}_{mod}, \hat{f}_{prop}, \hat{f}_{mod}, \hat{f}_{prop}, \hat{f}_{det}\}$  is constructed by chaining the building blocks 1 – 5:

$$1. u_{out} = \hat{f}_{mod}(u_{laser}, u_{obj}), \quad (9a)$$

$$2. u_{out} = \hat{f}_{prop}(u_{out}, d_{IC}), \quad (9b)$$

$$3. u_{out} = \hat{f}_{mod}(u_{out}, u_w), \quad (9c)$$

$$4. u_{out} = \hat{f}_{prop}(u_{out}, d_{CO}), \quad (9d)$$

$$5. I_{cam} = \hat{f}_{det}(u_{out}), \quad (9e)$$

## 3. RESULTS

We experimentally evaluate the performance of our MFO method on the open-source MNIST and FMNIST datasets in Subsec. A. We also demonstrate the MFO method on a novel application of stain-free classifying white blood cells in Subsec. B. We then illustrate MFO's advantage of memory- and computation-efficient training in Subsec. C.

### A. MFO outperforms hybrid training (HBT) in the real systems on the MNIST and FMNIST datasets

We conduct experiments on training the single-layer optical computing system (described in Fig. 3) on two classical image classi-

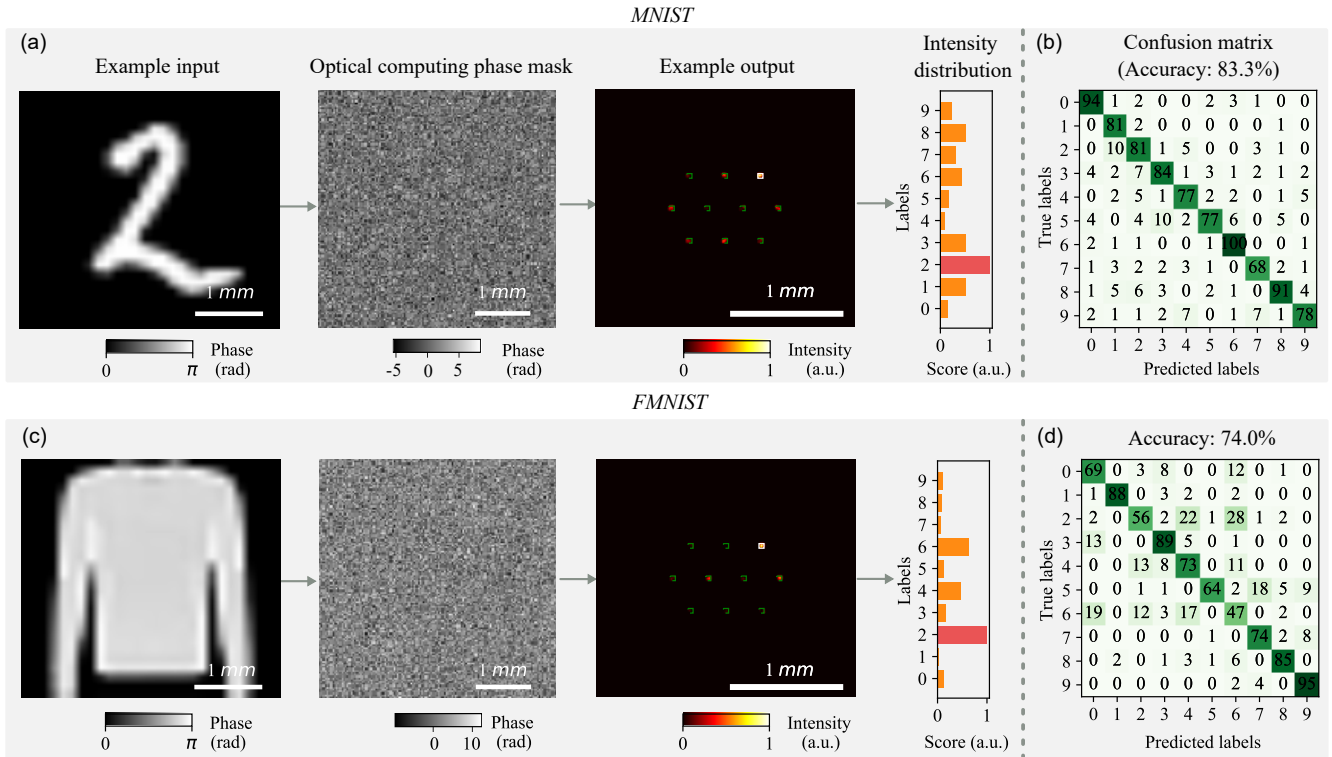


**Fig. 4. Visualization of experimental outputs and confusion matrices of the optical computing system trained with MFO.** (a) An input phase object digit ‘2’ from the MNIST dataset is modulated by the optical computing layer with weight  $w$  trained using MFO. The system correctly predicts the input as digit ‘2’, as the output image has the largest intensity at the region corresponding to digit ‘2’. We repeat this process on the whole train set. (b) The confusion matrix on the MNIST dataset and a training accuracy of 83.8%. (c) An example of a ‘pullover’ from the FMNIST dataset is correctly predicted. (d) Confusion matrix on the FMNIST dataset with a training accuracy of 74.0%.

fication datasets: MNIST [26] and FMNIST [27]. We include in silico SBT and in situ HBT methods as the comparison baselines. Table 2 quantitatively shows that our method achieves higher classification accuracy than the HBT and SBT methods on both datasets in the experiments. The SBT method performs poorly due to the gap between the simulator and the real system. The HBT method suffers from the bias between  $\hat{f}_{sys}$  and  $f_{sys}$  in the backward process, while the MFO bypasses the bias-sensitive modeling and updates gradients solely with  $f_{sys}$ . Figure 4 and Fig. S.3 visualize some experimental outputs and confusion matrices using the MFO and HBT methods, respectively.

See Supplement Sec. S.4 for the details of the MNIST and FMNIST datasets. Training details are in Supplement Sec. S.2. The detailed description of the HBT method is in Supplement Sec. S.6.

### B. Application: all-optical classification on cellular dataset.

For the first time, we demonstrate the capability of an optical computing system for stain-free cell analysis, trained by our MFO algorithm (Fig. 5). We work on the white blood cells (WBC), whose abnormal subtype percentages indicate the immune system’s malfunction or infectious disease [30, 31]. We include details of the WBC phase map dataset in Supplement Sec. S.4. Previously, researchers used machine learning methods to classify WBC subtypes, including monocyte, granulocyte, B cell, and T cell, by their morphology in a stain-free way [28, 32]. However, the analysis process is computationally

	MNIST			FMNIST		
	Train	Val	Test	Train	Val	Test
Ideal	92.7%	84.3%	82.2%	85.6%	79.9%	76.4%
SBT	81.9%	74.4%	69.3%	68.3%	64.1%	60.9%
HBT	81.9%	75.5%	72.8%	68.3%	68.7%	65.8%
MFO (Ours)	83.3%	77.8%	73.6%	74.0%	71.1%	70.4%

**Table 2. Performance comparison on MNIST and FMNIST datasets.** Results of the ideal mode are from the simulator, whose parameters are determined from experiments while we impose no misalignment on the simulator. The lower three rows are experimental results from SBT, HBT, and MFO. Our method outperforms the SBT and HBT methods on the MNIST and FMNIST datasets in experiments.

heavy and time-consuming. Here, we accelerate the stain-free cell analysis process via computing with light. Our MFO method strikes a training/validation/testing classification accuracy of 72.1%/73.3%/75.8% when classifying 4 types of WBC, exceeding that of the HBT method (Fig. 5c). Furthermore, Fig. 5d shows that the inference enabled by optical computing is almost instantaneous ( $\frac{d_{io}+d_{oc}}{c} = 1.4 \text{ ns}$ , where  $c$  is the speed of light), compared to the 1.7 ms of ResNet10, the electronic ma-

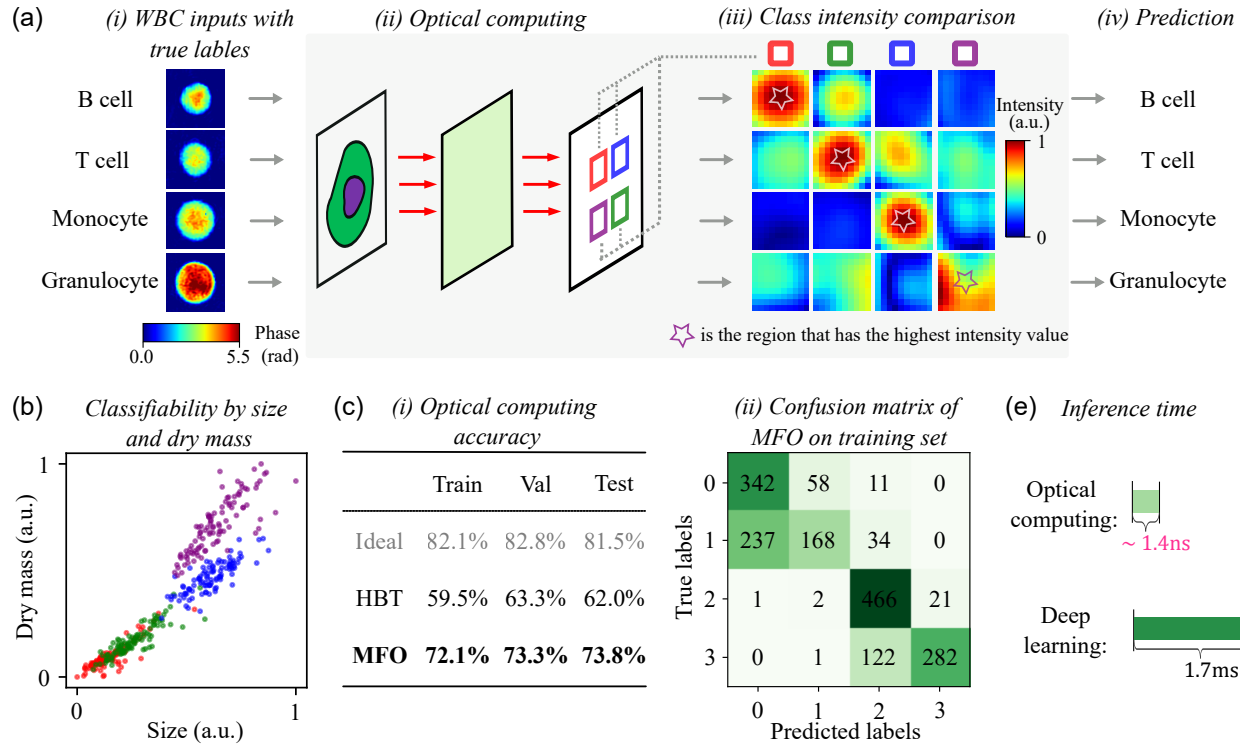


**Fig. 5. All optical cell classification enabled by MFO training.** (a) Our trained optical computing system classifies four WBC subtypes, including B cell, T cell, monocyte, and granulocyte, in a stain-free manner. The system uses the stain-free phase information of the WBCs (i) to perform optical classification optically (ii). The output plane of the system has different regions corresponding to different classes. We measure the intensity values in these regions (iii) and choose the class with the highest intensity as the prediction (iv). (b) shows that non-morphological features, including size and dry mass, cannot divide the four subtypes well. In contrast, (c)(i) shows the optical computing system trained with our MFO method can classify the WBC subtypes with a training/validation/testing accuracy of 72.1%/73.3%/73.8%, which is higher than that of the HBT method. (c)(ii) shows the confusion matrix of MFO results on the training set. (e) The optical computing system produces its output at the speed of light (1.4 ns). This is faster than ResNet10 [28, 29], which has an inference time of 1.7 ms.

chine learning model used in [28]. We currently need 1 more milliseconds of in silico computing of region intensities corresponding to different classes to obtain the prediction. Such a step can be skipped if we use single-photon avalanche diode (SPAD) [33] point detectors to count the corresponding regions' cumulative signals. Though for now, the performance of our single-layer linear optical computing system is not on par with the electronic neural network, which hits a testing classification accuracy of 90.5% [28], the potential of having ultra-high inference speed and  $> 70\%$  classification accuracy here point out an exciting direction on further increasing the complexity of our optical computing system to improve the absolute classification accuracy on classifying the cells.

### C. Advantage: memory- and computation-efficient training enabled by MFO.

Our MFO method has an advantage over other training algorithms regarding GPU time and memory efficiency, besides the predicting accuracy discussed in the previous subsection. The SBT and HBT methods compute  $\hat{f}_{sys}(x, w)$  and  $\nabla_w \hat{f}_{sys}$  (Fig. 1a) for each input  $x$  in silico, which requires a lot of in silico computation resources. In contrast, our MFO method executes the calculation of  $f_{sys}(x, w)$  in the light-speed real optical computing system, but not in the computation- and memory-heavy simulator  $\hat{f}_{sys}(x, w)$ . The only step of our MFO method that

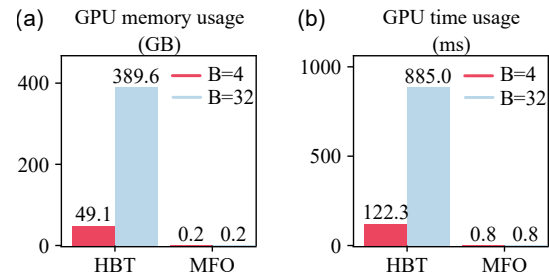


**Fig. 6. MFO saves in silico computing resources during training.** We compare the GPU memory (a) and time (b) consumption of HBT and MFO methods for training one batch of inputs with batch sizes of  $B = 4$  and  $B = 32$ . MFO is more efficient than HBT during the in situ training process in memory and time. Moreover, MFO's resource consumption does not increase as the batch size increases, unlike HBT.

consumes in silico computational resources is the one described in Eq. 7, where we calculate the score gradient. The in silico computational resources consumption in this step is low because it only scales with the dimension of  $w$  and has no relation to the complexity of the system's light transport  $\hat{f}_{sys}$ .

We compare our MFO method with HBT in GPU memory

and time usage in Fig. 6. Our MFO method requires far less GPU time and memory than the HBT method during the training.

## 4. DISCUSSION

### A. Limitation: MFO exhibits the curse of dimensionality

Our method is not without its limits. Our MFO training relies on Monte Carlo integration. It thus inherits the *curse of dimensionality* from the Monte Carlo integration [34]. That is, the number of samples  $M$  needed to estimate the integration in Eq. 6c with a given level of accuracy grows exponentially with respect to the  $H$ , the number of input variables (i.e., dimensionality) of the function. This is also discussed and alleviated with *variance reduction* in the previous Sec. 2C. However, the MFO strategy presented in this paper is still sample-inefficient, though unbiased and memory-efficient. We need to either limit the number of trainable parameters  $H$ , which is also the search space size  $H$  or sample a large number of varied optical computing weights  $\{w\}_{j=1}^M$  from distribution  $p(w_j|\theta)$  in every iteration to make MFO's gradient less noisy. The former limits the design DOF of our method, while the latter requires more executions on the real system, which prolongs the training time.

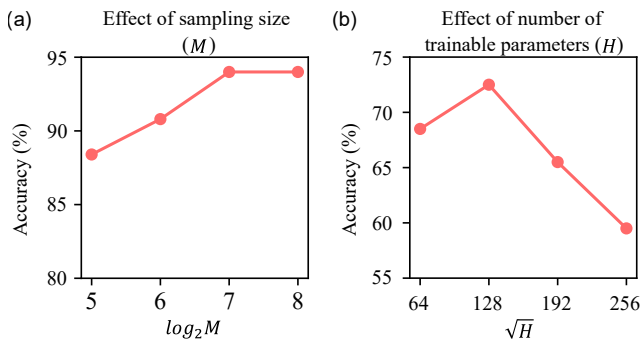


**Fig. 7. MFO exhibits the curse of dimensionality.** (a) When the sampling size of optical computing weights  $M$  rises from  $2^5 = 32$  to  $2^7 = 128$ , the training accuracy increases by 5.6%. However, increasing  $M$  from  $2^7 = 128$  to  $2^9 = 256$  does not improve accuracy. Here we fix the  $H$  as  $128^2$ . (b) MFO achieves the highest accuracy when  $H = 128^2$  under a sampling size  $M = 128$  while further enlarging  $H$  fails the result.

We quantitatively investigate the influence of this limitation in Fig. 7 with a small dataset, where we visualize how  $M$  and  $H$  impact the training performance MFO. In the investigation, we limit the training dataset to 200 samples from 4 FMNIST classes, as the MFO training in the simulator takes a long time. As shown in Fig. 7, MFO requires a  $M > 128$  to achieve a training accuracy of 94% given a search space size  $H = 128^2$ . Moreover, our MFO method catastrophically fails when increasing the search space size  $H$  beyond  $128^2$  when keeping the sampling size  $M$  fixed to 128.

### B. Future directions.

Exploring the scalability of the optical computing system to more complex optical structures, along with integrating more layers and non-linear activation functions, could potentially enhance absolute performance.

Future research could also consider employing more advanced techniques related to Monte Carlo integration to reduce the training variance discussed in the previous Subsec. A, which

we anticipate could substantially broaden the viable search space, thus further empowering the MFO approach. These include using more advanced sampling strategies [35] or integrating MFO with the SBT methods [36]. The latter makes a trade-off between the model bias and sampling variance.

### C. Conclusion

To conclude, our study underscores the effectiveness of a model-free strategy in training optical computing systems in situ, manifesting considerable potential in computational efficiency and reducing the simulation-to-reality performance gap. Although the study does not focus entirely on absolute image classification accuracy as it is based on a simple single-layer diffractive optical computing system, it shows relative improvements compared to the existing training strategies, indicating that our strategy is a potentially valuable approach. The model-agnostic nature of our technique may become even more beneficial when implemented in intricate optical systems, representing a robust and versatile alternative to current strategies. It promises a strong foundation for exploring and practically implementing optical computing in real-world applications such as high-speed cell analysis.

**Funding.** Hong Kong General Research Fund (14209521); Hong Kong Innovation and Technology Fund (ITS/178/20FP & ITS/148/20); Croucher Foundation (CM/CT/CF/CIA/0688/19ay).

**Acknowledgments.** We thank Cheng Zheng for the discussions in the early stage of the work.

**Author Contributions.** G.Z. conceived the project, derived the formulation, and built the backbone code and system. X.S. helped with the code writing and system setup and collected the simulation and experiment results. G.Z. and X.S. wrote the manuscript.

**Data availability.** Raw data underlying the results presented in this paper are not publicly available but can be obtained from the authors upon request.

**Code availability.** The code regarding this research will be released upon publication.

**Disclosures.** The authors declare no conflict of interest.

**Supplemental document.** See Supplement 1 for supporting content.

## REFERENCES

1. A. Maréchal and P. Croce, "Un filtre de fréquences spatiales pour lamélioration du contraste des images optiques," C. R. Acad. Sci. **237**, 607–609 (1953).
2. L. Cutrona, E. Leith, C. Palermo, and L. Porcello, "Optical data processing and filtering systems," IRE Transactions on Inf. Theory **6**, 386–400 (1960).
3. E. O'Neill, "Spatial filtering in optics," IRE Transactions on Inf. Theory **2**, 56–65 (1956).
4. P. Ambbs, "Optical computing: A 60-year adventure." Adv. Opt. Technol. (2010).
5. G. Wetzstein, A. Ozcan, S. Gigan, S. Fan, D. Englund, M. Soljačić, C. Denz, D. A. Miller, and D. Psaltis, "Inference in artificial intelligence with deep optics and photonics," Nature **588**, 39–47 (2020).
6. A. V. Lugt, "Signal detection by complex spatial filtering," IEEE Trans. Inf. Theory **10**, 139–145 (1964).
7. J. Zhou, H. Qian, C.-F. Chen, J. Zhao, G. Li, Q. Wu, H. Luo, S. Wen, and Z. Liu, "Optical edge detection based on high-efficiency dielectric metasurface," Proc. Natl. Acad. Sci. **116**, 11137–11140 (2019).
8. J. Chang, V. Sitzmann, X. Dun, W. Heidrich, and G. Wetzstein, "Hybrid optical-electronic convolutional neural networks with optimized diffractive optics for image classification," Sci. Reports **8**, 12324 (2018).

9. X. Lin, Y. Rivenson, N. T. Yardimci, M. Veli, Y. Luo, M. Jarrahi, and A. Ozcan, "All-optical machine learning using diffractive deep neural networks," *Science* **361**, 1004–1008 (2018).
10. M. Rafayelyan, J. Dong, Y. Tan, F. Krzakala, and S. Gigan, "Large-scale optical reservoir computing for spatiotemporal chaotic systems prediction," *Phys. Rev. X* **10**, 041037 (2020).
11. D. Verstraeten, B. Schrauwen, M. d'Haene, and D. Stroobandt, "An experimental unification of reservoir computing methods," *Neural Netw.* **20**, 391–403 (2007).
12. Y. Shen, N. C. Harris, S. Skirlo, M. Prabhu, T. Baehr-Jones, M. Hochberg, X. Sun, S. Zhao, H. Larochelle, D. Englund *et al.*, "Deep learning with coherent nanophotonic circuits," *Nat. Photonics* **11**, 441–446 (2017).
13. S. M. Buckley, A. N. Tait, A. N. McCaughan, and B. J. Shastri, "Photonic online learning: a perspective," *Nanophotonics* (2023).
14. D. E. Rumelhart, G. E. Hinton, and R. J. Williams, "Learning representations by back-propagating errors," *Nature* **323**, 533–536 (1986).
15. L. G. Wright, T. Onodera, M. M. Stein, T. Wang, D. T. Schachter, Z. Hu, and P. L. McMahon, "Deep physical neural networks trained with backpropagation," *Nature* **601**, 549–555 (2022).
16. J. Spall, X. Guo, and A. I. Lvovsky, "Hybrid training of optical neural networks," *Optica* **9**, 803–811 (2022).
17. A. Sludds, S. Bandyopadhyay, Z. Chen, Z. Zhong, J. Cochrane, L. Bernstein, D. Bunandar, P. B. Dixon, S. A. Hamilton, M. Streshinsky *et al.*, "Delocalized photonic deep learning on the internet's edge," *Science* **378**, 270–276 (2022).
18. D. Wierstra, T. Schaul, T. Glasmachers, Y. Sun, J. Peters, and J. Schmidhuber, "Natural evolution strategies," *The J. Mach. Learn. Res.* **15**, 949–980 (2014).
19. R. J. Williams, "Simple statistical gradient-following algorithms for connectionist reinforcement learning," *Reinf. Learn.* **8**, 229–256 (1992).
20. G. W. Brier *et al.*, "Verification of forecasts expressed in terms of probability," *Mon. Weather. Rev.* **78**, 1–3 (1950).
21. J. Schulman, N. Heess, T. Weber, and P. Abbeel, "Gradient estimation using stochastic computation graphs," *Adv. Neural Inf. Process. Syst.* **28** (2015).
22. S. Mohamed, M. Rosca, M. Figurnov, and A. Mnih, "Monte carlo gradient estimation in machine learning," *The J. Mach. Learn. Res.* **21**, 5183–5244 (2020).
23. Y. Song and S. Ermon, "Generative modeling by estimating gradients of the data distribution," *Adv. Neural Inf. Process. Syst.* **32** (2019).
24. J. Mei, W. Chung, V. Thomas, B. Dai, C. Szepesvari, and D. Schurmans, "The role of baselines in policy gradient optimization," *arXiv preprint arXiv:2301.06276* (2023).
25. M. Born and E. Wolf, *Principles of optics: electromagnetic theory of propagation, interference and diffraction of light* (Elsevier, 2013).
26. L. Deng, "The mnist database of handwritten digit images for machine learning research," *IEEE Signal Process. Mag.* **29**, 141–142 (2012).
27. H. Xiao, K. Rasul, and R. Vollgraf, "Fashion-mnist: a novel image dataset for benchmarking machine learning algorithms," *arXiv preprint arXiv:1708.07747* (2017).
28. X. Shu, S. Sansare, D. Jin, X. Zeng, K.-Y. Tong, R. Pandey, and R. Zhou, "Artificial-intelligence-enabled reagent-free imaging hematology analyzer," *Adv. Intell. Syst.* **3**, 2000277 (2021).
29. K. He, X. Zhang, S. Ren, and J. Sun, "Identity mappings in deep residual networks," in *Computer Vision—ECCV 2016: 14th European Conference, Amsterdam, The Netherlands, October 11–14, 2016, Proceedings, Part IV 14*, (Springer, 2016), pp. 630–645.
30. B. J. Bain, *Blood cell morphology in health and disease* (Elsevier, 2017), pp. 61–92.
31. G. DOnofrio and G. Zini, *Blood and Bone Marrow Cells* (2015), pp. 1–87.
32. M. Nassar, M. Doan, A. Filby, O. Wolkenhauer, D. K. Fogg, J. Piasecka, C. A. Thornton, A. E. Carpenter, H. D. Summers, P. Rees, and H. Hennig, "Label-free identification of white blood cells using machine learning," *Cytom. Part A* **95**, 836–842 (2019).
33. C. Bruschini, H. Homulle, I. M. Antolovic, S. Burri, and E. Charbon, "Single-photon avalanche diode imagers in biophotonics: review and outlook," *Light. Sci. & Appl.* **8**, 87 (2019).
34. R. Bellman and R. Kalaba, "On adaptive control processes," *IRE Transactions on Autom. Control.* **4**, 1–9 (1959).
35. R. E. Caflisch, "Monte carlo and quasi-monte carlo methods," *Acta Numer.* **7**, 1–49 (1998).
36. V. Kurenkov and B. Maksudov, "Guiding evolutionary strategies by differentiable robot simulators," *arXiv preprint arXiv:2110.00438* (2021).
37. T. Zhou, X. Lin, J. Wu, Y. Chen, H. Xie, Y. Li, J. Fan, H. Wu, L. Fang, and Q. Dai, "Large-scale neuromorphic optoelectronic computing with a reconfigurable diffractive processing unit," *Nat. Photonics* **15**, 367–373 (2021).
38. S. Choi, M. Gopakumar, Y. Peng, J. Kim, M. O'Toole, and G. Wetzstein, "Time-multiplexed neural holography: a flexible framework for holographic near-eye displays with fast heavily-quantized spatial light modulators," in *ACM SIGGRAPH 2022 Conference Proceedings*, (2022), pp. 1–9.
39. A. B. Ayoub and D. Psaltis, "High speed, complex wavefront shaping using the digital micro-mirror device," *Sci. Reports* **11**, 18837 (2021).
40. D. Blinder, T. Birnbaum, T. Ito, and T. Shimobaba, "The state-of-the-art in computer generated holography for 3d display," *Light. Adv. Manuf.* **3**, 572–600 (2022).
41. E. Riba, D. Mishkin, D. Ponsa, E. Rublee, and G. Bradski, "Kornia: an open source differentiable computer vision library for pytorch," in *Proceedings of the IEEE/CVF Winter Conference on Applications of Computer Vision*, (2020), pp. 3674–3683.

## SUPPLEMENTS

### Contents

S.1	Reproducibility of the hardware system . . . . .	9
S.1.1	Hardware details of the optical computing system. . . . .	9
S.1.2	Parameters of the optical computing system . . . . .	9
S.2	Training details . . . . .	9
S.2.1	Computing resources. . . . .	9
S.2.2	Training parameters and time of simulation . . . . .	9
S.2.3	Training process for experiments . . . . .	10
S.3	Compare the overall training time of MFO and HBT . . . . .	10
S.4	Dataset details . . . . .	11
S.5	Calibration of the system . . . . .	11
S.5.1	Calibrate propagation distance $z$ using holography. . . . .	12
S.5.2	Homography estimation among multiple planes. . . . .	12
S.5.3	Rebuild the simulator with homography estimation in the loop. . . . .	12
S.6	Baseline method – Hybrid training. . . . .	12

### S.1. Reproducibility of the hardware system

#### S.1.1. Hardware details of the optical computing system.

Table S.1 lists models of critical components used in our home-built optical computing system. Table S.2 further provides dimensions and frame rates of programmable optical devices (i.e., SLM1, SLM2 and DMD) and cameras involved in this work. The definition of the modulation area is shown in Fig. S.1.

Device	Part number	Manufacturer
SLM1	PLUTO	Holoeye
SLM2	GAEA	Holoeye
DMD*	DLPLCR6500EVM or DLP7000	TI
Camera	BFS-U3-13Y3C-C	Teledyne FLIR
BS	HBS11-025-50-VIS	Hengyang Optics
Polarizer	CCM5-PBS201/M	Thorlabs

\* The DMD is not experimentally used. We use its parameters to compare the MFO training time.

**Table S.1.** Models of key components used in our optical computing system.

Device	Pitch size ( $\mu\text{m}$ )	Full shape (pixels)	Modulation area shape (pixels)	Refreshing rate (FPS)
SLM1	8	1080 × 1920	512 × 512	25*
SLM2	3.74	2160 × 3840	1248 × 1248	30*
DMD	7.6	1080 × 1920	512 × 512	1440 [37]
Camera	8	1024 × 1280	512 × 512	170

\* We experimentally get 25 or 30 FPS in our self-written Python programs.

**Table S.2.** Dimensions and frame rates of our experiments' programmable optical devices and cameras.

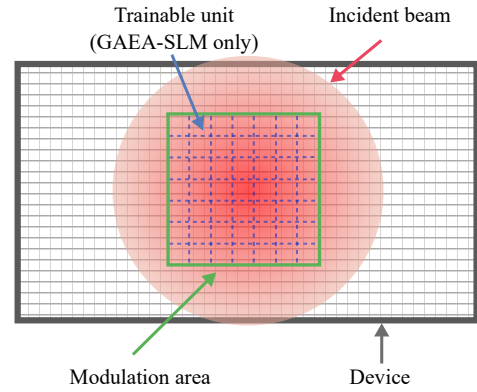


**Fig. S.1.** Optical computing modulation area. In our experiments, the incident laser beam cannot fully illuminate the entire working area of the programmable optical devices and cameras. To ensure efficient modulation, we create a smaller optical computing modulation area for each device, fully covered by the incident beam. Pixel values outside this area are set to zero, allowing only those within the area to be configurable. Additionally, we divide the SLM2 modulation area - the optical computing layer - into uniformly valued partitions. Each partition represents a trainable parameter of  $w$ .

#### S.1.2. Parameters of the optical computing system

The optical computing weight  $w$  comprises  $H = 128^2$  trainable parameters, and we use sampling size  $M = 128$  throughout the paper if not specifically specified. We obtain the classification prediction of the optical computing system by comparing the intensities of different regions in the output layer [9, 37], as illustrated in Fig. S.2.

### S.2. Training details

#### S.2.1. Computing resources.

We evaluate our method both in simulation and in experiments. The simulation runs on a high-end Linux server. Physical experiments are conducted with a Windows desktop. Table S.3 shows the Windows desktop and Linux server configurations.

	Server (Simulation)	Desktop (Experiments)
CPU	Intel Xeon Silver 4210R [×2]	Intel Core i7-7700
GPU	Nvidia A6000 [×2]	Nvidia TITAN XP
GPU memory	48GB [×2]	12GB
RAM	192GB	32GB
Operating system	Ubuntu 18.04	Windows 10
Graphic interface	No	Yes

**Table S.3.** Configurations of our server and desktop.

#### S.2.2. Training parameters and time of simulation

The training parameters and time of simulation are shown in Table S.4. In MFO simulation with a sampling size of optical computing weights as  $M = 128$ , we can only process one input at a time due to GPU memory limitation. Training MFO is much slower than training the SBT since MFO requires  $M = 128$  sampled variants, and thus the forward computing in the simulator takes time.

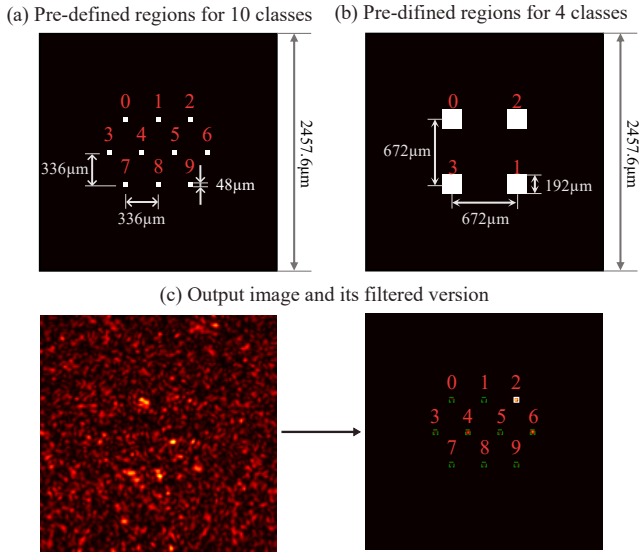


**Fig. S.2. Getting classification prediction of the optical computing system.** We obtain the classification prediction of the optical computing system by taking an image with the camera and summing up the pixel values in different regions to get the intensity of each class. The class with the highest intensity is the predicted class of the system. (a) shows the pre-defined regions for 10 classes, we set the regions to have a size of  $48\mu\text{m} \times 48\mu\text{m}$  and the distance between two regions is  $336\mu\text{m}$ . (b) shows pre-defined regions for 4 classes, we set the regions to have a size of  $192\mu\text{m} \times 192\mu\text{m}$  and the distance between two regions is  $672\mu\text{m}$ . (c) shows an example of a captured image (lower left) and its filtered version (lower right). The filtered version sets pixel values outside the class regions to zero for clearer visualization.

	SBT	MFO
Sampling size $M$	NAN	128
Parallel computing batch size	32	1
Batch size $B$	32	32
Optimizer	Adam	SGD
Learning rate	0.01	2
Per-epoch training time	17s	4m47s

**Table S.4. Training parameters and time for simulation.** MFO is slow in simulation as the computational-intensive simulations substitute the light-speed forward optical computation and sampling.

### S.2.3. Training process for experiments

The training process for MFO and HBT experiments consists of getting optical computing system output  $f_{\text{sys}}(x, w)$  and performing in silico gradient calculation and parameter update. Experiment workflow S.1 shows how to get  $\{f_{\text{sys}}(x_i, w)\}_{i=1}^B$  in the HBT experiment. In the MFO experiment, we use different experiment workflows to get  $\{f_{\text{sys}}(x_i, w_j)\}_{i=1, j=1}^{B, M}$  depending on the specific devices used as input and optical computing layers. If we use SLM1 and SLM2 ( $\text{responsetime}_I > \text{responsetime}_O$ ), we use Experiment workflow S.2 for the sake of a shorter waiting time. If we use DMD and SLM2 ( $\text{responsetime}_I > \text{responsetime}_O$ ), we use Experiment workflow S.3.  $B$  is the batch size,  $M$  is the sampling size,  $\text{responsetime}_I$  is the input layer device response time and  $\text{responsetime}_O$  is the optical computing layer device response time. The training parameters and time

for MFO and HBT are shown in Table S.5.

**Experiment workflow S.1.** Acquiring  $\{f_{\text{sys}}(x_i, w)\}_{i=1}^B$  in HBT experiment.

- 1: **Input:** A batch of classification dataset  $\mathcal{D}_b = \{x_i, y_i\}_{i=1}^B$  with batch size  $B$ , optical computing weight  $w$ , optical computing system  $f_{\text{sys}}$ , input layer device response time  $\text{responsetime}_I$ , optical computing layer device response time  $\text{responsetime}_O$ .
- 2: **Output:** Optical computing system output  $\{f_{\text{sys}}(x_i, w)\}_{i=1}^B$ .
- 3: Refresh  $w$  on the optical computing layer.
- 4: ▷ Wait  $\text{responsetime}_O$ .
- 5: **for**  $i$  in range  $B$  **do**
- 6:   Display  $x_i$  on input layer.
- 7:   ▷ Wait  $\text{responsetime}_I$ .
- 8:   Capture  $f_{\text{sys}}(x_i, w)$  with camera.
- 9: **Total waiting time:**  $\text{responsetime}_O + B \times \text{responsetime}_I$ .

**Experiment workflow S.2.** Acquiring  $\{f_{\text{sys}}(x_i, w_j)\}_{i=1, j=1}^{B, M}$  in MFO experiment when optical computing layer device has a short response time.

- 1: **Input:** A batch of classification dataset  $\mathcal{D}_b = \{x_i, y_i\}_{i=1}^B$  with batch size  $B$ , a group of sampled optical computing weights  $\{w_j\}_{j=1}^M$ , optical computing system  $f_{\text{sys}}$ , input layer device response time  $\text{responsetime}_I$ , optical computing layer device response time  $\text{responsetime}_O$ .
- 2: **Output:** Optical computing system output  $\{f_{\text{sys}}(x_i, w_j)\}_{i=1, j=1}^{B, M}$ .
- 3: **for**  $i$  in range  $L$  **do**
- 4:   Display  $x_i$  on input layer.
- 5:   ▷ Wait  $\text{responsetime}_I$ .
- 6:   **for**  $j$  in range  $M$  **do**
- 7:     Refresh  $w_j$  on the optical computing layer.
- 8:     ▷ Wait  $\text{responsetime}_O$ .
- 9:     Capture  $f_{\text{sys}}(x_i, w_j)$  with camera.
- 10: **Total waiting time:**  $B \times M \times \text{responsetime}_O + B \times \text{responsetime}_I$

We stop the training process when the validation loss does not decrease for 10 epochs in both simulation and real system experiments. We choose the checkpoint with the lowest validation loss and use it to evaluate the test set. In Sec.4 A, however, we apply a different rule to make the model overfit on the training dataset. We stop the training process after 50 epochs of no decrease in the training loss when testing the effect of sampling size and after 10 epochs when testing the effect of number of trainable parameters, due to training time constraints.

### S.3. Compare the overall training time of MFO and HBT

We use the optical computing layer based on the conventional phase-SLM, with an experimentally achievable refreshing rate of about 30 FPS (see Tab. S.2). For now, refreshing weights  $w$  on the optical computing layer consumes far more time than the light-speed computation of  $f_{\text{sys}}(x, w)$ . Given the current refreshing rate of optical computing layer, the overall training time of the MFO is larger than that of the HBT (see Tab. S.5). This time bottleneck can be alleviated when substituting the conventional phase-SLM with the fast ones, such as the Heavily-quantized Spatial Light Modulators [38] or the digital micromirror devices [39], which exhibit thousands of FPS. In such a way, we

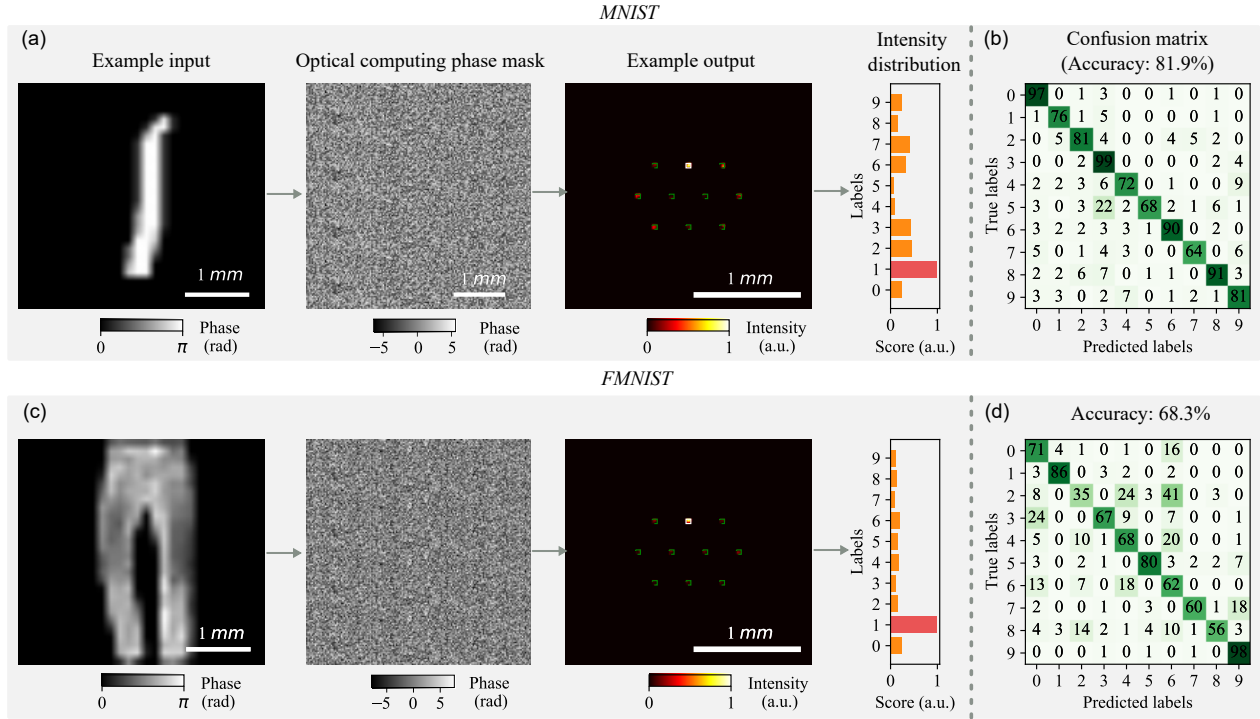


**Fig. S.3.** Example outputs and confusion matrices of the optical computing system trained with HBT optimization. (a) the optical computing system trained with HBT correctly predicts an input phase object digit ‘1’ from the MNIST dataset. In (b), we show we achieve an accuracy of 81.9% on the MNIST training dataset. (c) an example of ‘trouser’ from the FMNIST training dataset is correctly predicted. (d) shows that the accuracy on the FMNIST training dataset is 68.3%.

**Experiment workflow S.3.** Acquiring  $\{f_{sys}(x_i, w_j)\}_{i=1, j=1}^{B, M}$  in MFO experiment when input layer device has a short response time.

- 1: **Input:** A batch of classification dataset  $\mathcal{D}_b = \{x_i, y_i\}_{i=1}^B$  with batch size  $B$ , a group of sampled optical computing weights  $\{w_j\}_{j=1}^M$ , optical computing system  $f_{sys}$ , input layer device response time  $responsetime_I$ , optical computing layer device response time  $responsetime_O$ .
- 2: **Output:** Optical computing system output  $\{f_{sys}(x_i, w_j)\}_{i=1, j=1}^{B, M}$ .
- 3: **for**  $j$  in range  $M$  **do**
- 4: Refresh  $w_j$  on the optical computing layer
- 5: ▷ Wait  $responsetime_O$
- 6: **for**  $i$  in range  $L$  **do**
- 7: Load  $x_i$  to input layer
- 8: ▷ Wait  $responsetime_I$
- 9: Capture  $f_{sys}(x_i, w_j)$  with camera
- 10: **Total waiting time:**  $M \times responsetime_O + B \times M \times responsetime_I$

can significantly reduce the overall training time of our method (Tab. S.6).

#### S.4. Dataset details

**MNIST and FMNIST** We randomly split 2000 digits (200 per class) from the MNIST or FMNIST dataset into training and validation sets of equal size. We additionally use 1000 digits (100 per class) for testing.

	MFO	HBT
Batch size $L$	32	4
Sampling size $M$	128	None
Optimizer	SGD	Adam
Learning rate	100	0.01
<i>In silico</i> computation time*	6s	2m16s
Device waiting time for getting $f_{sys}(x, w)$ *	1h56m01s	2m18s
Total training time*	1h56m07s	4m34s

\* Time per epoch.

**Table S.5.** Training parameters and training time for experiments. As the optical computing time is negligible, the time here consists mainly of SLM pattern refreshing time and camera exposure time. MFO requires evaluating a lot of masks in the real system and thus cannot

**WBC dataset** The WBC phase image dataset [28] has four classes of cells: granulocyte, monocyte, B lymphocyte, and T lymphocyte. Table S.7 gives the number of cells in each class.

#### S.5. Calibration of the system

We calibrate the optical computing system shown in Fig. 3. The calibration is critical for reproducing baseline methods that rely on the model  $\hat{f}_{sys}$  as tiny misalignment between multiple planes will hugely degrade the performance, as we have shown in Fig. 2. Our digital alignment consists of estimating 2 sets of parameters: lengths  $\{d_{IO}, d_{CO}\}$  and homography transformations  $\{H_{IO}, H_{CO}\}$ . Specifically,  $H_{IO}$  is the projective transformation between the input layer and output layer,  $d_1 + d_2$  is the

	MFO	HBT
<i>In silico</i> computation time*	6s	2m16s
Device waiting time for getting $f_{sys}(x, w)$ *	3m43s	2s
Total training time*	3m49s	2m18s

\* Time for one epoch.

**Table S.6. Using Digital Micromirror Device (DMD) as the input layer can speed up the MFO training.** We only estimate the training time by calculation when using DMD as the input layer device and SLM2 as the optical computing layer device. With  $N = 1000$ ,  $B = 32$ , and  $M = 128$ , we use the same *in silico* time as in Tab. S.5. While getting  $f_{sys}(x, w)$ ,  $responsetime_I = 1000/1440\text{Hz} = 0.69\text{ms}$ ,  $responsetime_O = 1000/30\text{Hz} = 33\text{ms}$ . We use Experiment workflow. S.1 in the HBT experiment and Experiment workflow. S.3 in the MFO experiment. The total device waiting time for each batch is  $33\text{ms} + 32 \times 0.69\text{ms} = 55.08\text{ms}$  in the HBT experiment and  $128 \times 33\text{ms} + 32 \times 128 \times 0.69 = 7050.24\text{ms}$  in the MFO experiment, except for the last batch with 8 samples, which has a device waiting time of  $33\text{ms} + 8 \times 0.69\text{ms} = 38.52\text{ms}$  and  $128 \times 33\text{ms} + 8 \times 128 \times 0.69 = 4930.56\text{ms}$ , respectively. There are 32 batches in total. The total per-epoch device waiting time for getting  $f_{sys}(x, w)$  in the HBT experiment is about  $31 \times 55.08\text{ms} + 38.52\text{ms} \approx 2\text{s}$ , while in the MFO experiment it is about  $31 \times 7050.24\text{ms} + 4930.56\text{ms} \approx 3\text{m}43\text{s}$ .

	Training set	Validation set	Testing set
Granulocyte	465	100	100
Monocyte	513	100	100
B lymphocyte	437	100	100
T lymphocyte	330	100	100
Total	1745	400	400

**Table S.7. Number of cells of each class in the WBC dataset.**

corresponding distance,  $H_{CO}$  is the projective transformation between the optical computing layer and output layer, and  $d_2$  is the corresponding distance.

### S.5.1. Calibrate propagation distance $z$ using holography.

We first use free-space holography [40] to calibrate the distance  $d$  between planes. We concatenate the building blocks Eq. 8a and 8c and construct a free-space holography simulator  $\hat{f}_{holo} = \{\hat{f}_{prop}, \hat{f}_{det}\}$ . The input to the holography simulator is  $u_{in} = e^{i\phi_{holo}}$  and  $d$ , where  $\phi_{holo}$  is the pre-calculated phase that generates the hologram, while  $d$  is the distance to optimize. Calculation of  $\phi_{holo}$  is achieved by extracting the phase of Fourier transform of the target obj  $I_{target}$ :

$$\phi_{holo} = \text{angle}(\mathcal{F}(\sqrt{I_{target}})) \quad (\text{S.1})$$

Then we upload the  $\phi_{holo}$  onto the real SLM with the Holoeye Slideshow software, add various defocus phase masks corresponding to various  $d$ , visually compare the quality of the output hologram and select the best fit  $d$  as the calibrated distance.

### S.5.2. Homography estimation among multiple planes.

Homography is a linear transformation between corresponding points in two images with an 8 degree of freedom [41]. It

is solved by minimizing dense photometric loss or by feature matching. Our experiment has two SLMs and a camera (Fig. 3). Since directly calibrating  $H_{IC}$ , the transformation between the two SLMs, is infeasible as we cannot put the camera on any plane of these two SLMs; we calibrate their transformations to the output plane (the camera plane), respectively. Take the estimation of photometric-based homography between the input layer and the output layer as an example. The objective function is:

$$H_{IO}^* = \arg \min_{H_{IO}} \mathcal{L}_{holo}(\sqrt{I_{target}} - \text{warp}(|\hat{f}_{prop}(u_{in}, d_{IO})|)), \quad (\text{S.2})$$

where  $\text{warp}$  is the homography warpper given the homography estimation  $H_{IO}$ . We solve this objective function with auto-differentiation [41].

### S.5.3. Rebuild the simulator with homography estimation in the loop.

In the previous subsection, we discuss estimating the homography transformation between planes in the real system.

To incorporate the calibrated homography matrices into our system simulator  $\hat{f}_{sys}$ , we rebuild the simulator with three virtual propagators instead of two. The latter is discussed in the main text and depicted in Fig S.4(a). We use a 3-layer simulator because the homography wrapper  $\text{warp}$  and the wave propagator  $\hat{f}_{prop}$  are not commutative. In other words:

$$\text{warp}(\hat{f}_{prop}(u_{in}, d_{IO}), H_{IO}) \neq \hat{f}_{prop}(\text{warp}(u_{in}, H_{IO}), d_{IO}). \quad (\text{S.3})$$

A sketch of the rebuilt simulator is in Fig. S.4(b). We introduce a virtual output plane  $O_{virtual}$  into the simulator so that we can incorporate the homography estimations  $H_{IO}$  and  $H_{CO}$  into the simulation loop. Since the homography matrix is estimated at the output planes of the optical propagator, the settings in Fig. S.4(b) enable the use of homography matrix at the output planes of the propagator, which cannot be done via using the original simulator in Fig. S.4(a).

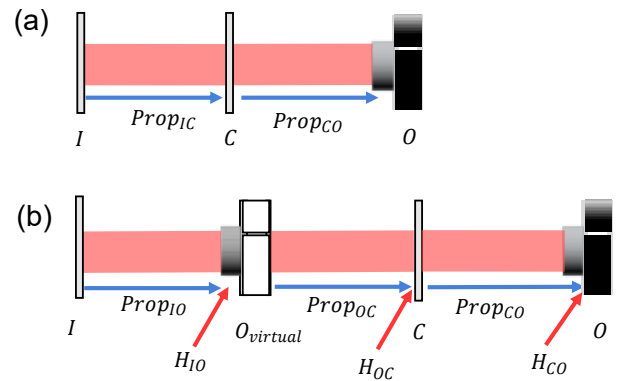


**Fig. S.4.** We rebuild the original simulator as sketched in (a) into the three-propagator-based simulator in (b) in order to incorporate the homography estimations into the simulator.  $O_{virtual}$  denotes the virtual camera plane, which does not exist in the real system. Here we use  $O_{virtual}$  to help calibrate the system.

### S.6. Baseline method – Hybrid training.

We include the hybrid training (HBT)/physics-aware training as one of the baseline methods to compare [15, 16]. The philosophy of hybrid training is simple: when updating the optical computing system, we use the real system to do the forward pass to get

the value of the objective function  $J(w)$ :

$$J(w) = \frac{1}{N} \sum_{i=1}^N \mathcal{L}(f_{sys}(x_i; w), y_i). \quad (\text{S.4})$$

In the backward update pass, we substitute the  $f_{sys}$  with its differentiable simulator  $\hat{f}_{sys}$  and update the weights  $w$  via:

$$w = w + \alpha \frac{\partial J(w)}{\partial \hat{f}_{sys}} \frac{\partial \hat{f}_{sys}}{w}. \quad (\text{S.5})$$

This trick enables the backward pass in the biased while differentiable simulator  $\hat{f}_{sys}$ . The critical difference between the hybrid training (HBT) method and the simulator-based training (SBT) is that the former does the forward pass in the real system  $f_{sys}$  while the latter conducts both passes in the simulator  $\hat{f}_{sys}$ .

We visualize some experimental outputs and confusion matrices using HBT in Fig. S.3.